



MODELING THE SHOCK RESPONSE OF SILICON CARBIDE, BORON CARBIDE AND TITANIUM DIBORIDE

A. M. RAJENDRAN and D. J. GROVE

Materials Directorate, Army Research Laboratory, Aberdeen Proving Ground, MD 21005, U.S.A.

(Received 12 April 1995; in revised form 30 October 1995)

Summary—An advanced constitutive model is used to describe the shock and high strain rate behaviors of silicon carbide, boron carbide, and titanium diboride under impact loading conditions. The model's governing equations utilize a set of microphysically based constitutive relationships to describe the deformation and damage processes of ceramics. The total strain is decomposed into elastic, plastic, and microcracking components. The plastic strain components are calculated using conventional viscoplastic equations. The strain components due to microcracking utilize relationships derived from a penny shaped crack in an infinite elastic solid. The main features of the model include degradation of strength and stiffness under both compressive and tensile loading conditions. When loaded above the Hugoniot elastic limit (HEL), the strength is limited by the strain rate dependent strength equation. However, below the HEL, the strength variation with respect to strain rate and pressure is modeled through microcracking relationships, assuming no plastic flow. The ceramic model parameters were determined using plate impact experimental data. Copyright © 1996 Elsevier Science Ltd.

Keywords: ceramic, modeling, shock, high strain rate, fracture, silicon carbide, titanium diboride, hydrocode.

1. INTRODUCTION

Ceramic materials are increasingly being used in armor elements, engine turbine blades and other structural elements because of their enhanced dynamic compressive strength and high temperature properties. Understanding of ceramic behavior under impact loading conditions is essential in the design of improved impact resistant materials for dynamic structural and armor applications. For this purpose, several impact/shock-wave-propagation experimental techniques are available. Experimental data are often used in the development of constitutive/damage models to describe the complex impact behavior of ceramic materials. Increased use of advanced finite element/difference computer codes in armor/anti-armor design analyses requires development and implementation of dependable and realistic material models in these codes. This requirement is essential for accurately describing the complex behaviors of advanced materials such as ceramics and glass fiber-reinforced plastic materials.

One of the most important aspects in the development of advanced material models is the determination of the model constants for use in numerical simulations of impact problems. In general, most of the more advanced models lack this aspect, thus precluding their usefulness in finite element simulations. Recently, Rajendran [1, 2] presented an internal state variable based constitutive model to describe the impact behavior of ceramic materials. The main objective of this paper is to provide the details of a technique that can be used to systematically evaluate this model's constants for various ceramics.

The ceramic constitutive model assumes the following:

- pre-existing randomly distributed flaws in the ceramic;
- plastic flow in the ceramic when shocked above the HEL;
- no plastic flow in tension;
- degradation of elastic moduli under both compression and tension; and
- pulverization of the ceramic under compressive loading, when the accumulated crack density reaches a value of 0.75.

The pre-existing flaws (microcracks) are activated according to a generalized Griffith criterion, and their growth rate is governed by a fracture mechanics based relationship.

There are three constants that characterize the virgin ceramic: number of microflaws (N_0^*), initial size of the largest flaw (a_0), and the dynamic coefficient of friction (μ). For damage evolution, the model

has two constants: crack growth factor (n_1) and crack growth exponent (n_2). These two loading-state dependent constants may take on different values under tension and compression. For most ceramics, n_1 and n_2 are assumed to be equal to 1 during tensile crack growth. The mode I fracture toughness (K_{1C}) is determined through direct measurements or from handbooks. At present, representative values for the model parameters were determined based on the model's ability to reproduce measured stress/velocity profiles from plate impact experiments.

This work describes the modeling of three armor ceramics: titanium diboride (TiB_2), silicon carbide (SiC), and boron carbide (B_4C). The experimental data of Kipp and Grady [3] were employed in the modeling efforts. Steinberg [4], Johnson and Holmquist [5], and Addressio and Johnson [6] also employed the Kipp and Grady data in their modeling efforts. Recently, Mandell and Henninger [7] evaluated the ceramic models of Steinberg and Johnson–Holmquist using the MESA code [8]. In the following section, the salient features of the ceramic model are briefly described. In Section 3 the capabilities of the model in reproducing the velocity interferometer (VISAR) data from the plate impact experiments are shown. The various features of the ceramic model are explored through a series of simulations in which the model constants were systematically varied.

2. DESCRIPTION OF THE MODEL

Rajendran presented a detailed description of the ceramic model in a recent volume of this journal [1]. For completeness, a brief description of this ceramic model is provided in this paper. The model assumes the existence of flaws (microcracks) in the virgin material. Therefore, the model does not require any microcrack nucleation criterion. The existing flaws are activated (extended) when the stress state satisfies a generalized Griffith's criterion. The effect of crack interaction due to coalescence is neglected. When the accumulating crack density reaches a critical value, the model assumes pulverization of the ceramic.

2.1. Constitutive relationships

The ceramic model assumes strains due to:

- (1) elastic and dislocation-based plastic deformation;
- (2) microcrack opening and sliding; and
- (3) pore collapsing.

In this section, the stress–strain relationship for a microcracked material is briefly discussed. The total strain is decomposed into elastic (ϵ_{ij}^e) and plastic strains (ϵ_{ij}^p) as,

$$\epsilon_{ij} = \epsilon_{ij}^e + \epsilon_{ij}^p \quad (1)$$

where the elastic strain consists of the elastic strain of the intact matrix material and the strain due to crack opening/sliding. The plastic strains associated with pore collapsing are modeled using the equations derived by Rajendran *et al.* [9] for a porous ductile aggregate. Plastic flow and pore collapse are assumed to occur in the ceramic only when the applied pressure exceeds the pressure at the Hugoniot elastic limit (HEL).

The elastic stress–strain equations for the microcracked aggregate material are given by,

$$\sigma_{ij} = M_{ijkl}\epsilon_{kl}^e \quad (2)$$

Following Margolin's work [10], the components of the stiffness tensor M are described by Rajendran in Ref. [1]. The total stress components (σ_{ij}) are decomposed into deviatoric stress components (S_{ij}) and pressure (P):

$$\sigma_{ij} = S_{ij} + P\delta_{ij} \quad (3)$$

The pressure is calculated through the Mie–Grüneisen equation of state which is given by,

$$P = [P_H(1 - 0.5\Gamma\eta) + \Gamma\rho_0(I - I_0)] \quad (4)$$

where

$$P_H = K_v(\beta_1\eta + \beta_2\eta^2 + \beta_3\eta^3). \quad (5)$$

In the above expressions, $\eta (= \rho/\rho_0 - 1)$ is the elastic volumetric compressive strain, $\beta_1, \beta_2,$ and β_3 are empirical parameters, Γ is the Mie–Gruneisen parameter, ρ_0 is the material's initial density, I_0 is the initial value of internal energy, I is the current internal energy, and K_γ is the ratio of the microcracks–degraded bulk modulus to the intact bulk modulus. This ratio reduces from 1 to 0 as the elastic properties degrade with microcracking.

The elastic deviatoric stress–strain relationship is given by,

$$S_{ij} = 2G(e_{ij} - e_{ij}^p) \quad (6)$$

where e_{ij} are the total deviatoric strains and G is the degraded shear modulus. The intact bulk and shear moduli are adjusted for porosity (f) using correction factors as suggested by Johnson [11]. The initial porosity (f_0) is a material model constant. The porosity is assumed to decrease due to pore collapsing at pressures above the HEL.

When the estimated von-Mises stress ($\sqrt{3J_2}$) exceeds the compressive strength (Y) measured from the plate impact experiments, plastic flow is assumed and the deviatoric stresses are determined by satisfying the von-Mises criterion ($Y = \sqrt{3J_2}$). The strain rate dependent compressive strength is described by a simple relationship:

$$Y = C_1(1 + C_3 \ln \dot{\epsilon}) \quad (7)$$

where C_1 and C_3 are model constants and $\dot{\epsilon}$ is the applied strain rate. The constant C_1 is assumed to be equal to Y_{HEL} , calculated from:

$$C_1 = Y_{\text{HEL}} = \frac{\sigma_{\text{HEL}}}{\left(\frac{K}{2G} + \frac{2}{3}\right)} \quad (8)$$

where σ_{HEL} is the maximum amplitude of the elastic shock. The constant C_3 is calibrated by matching the ‘plastic wave’ portion of the stress or velocity profiles of conventional planar plate impact experiments.

2.2. Definition of damage

In the ceramic model, microcrack damage is measured in terms of a dimensionless microcrack density γ which is defined as,

$$\gamma = N_0^* a^3. \quad (9)$$

N_0^* is the average number of microflaws per unit volume and a , the maximum microcrack size, is treated as an internal state variable. The initial values of these two parameters are material model constants. Experimental measurements to determine the initial number of microflaws in a unit volume and the initial maximum size of the microcracks are very difficult and tedious. These values are usually guessed, and calibration is based on the model's ability to reproduce the measured stress/velocity histories in plate impact experiments.

Microcracks are assumed to extend when the stress state satisfies a generalized Griffith criterion [12, 13]. This criterion requires the fracture toughness K_{1c} as well as a dynamic frictional coefficient μ as model parameters. During microcrack extension, the crack density (γ) increases and stress relaxation occurs. Since N_0^* is assumed to be a constant in the model, any increase in γ is entirely due to microcrack growth (increase in a).

2.3. Damage growth model

The crack extension (damage evolution) law is derived from a fracture mechanics based relationship [14] for a single crack propagation under dynamic loading conditions:

$$\dot{a} = \begin{cases} 0 & , \quad G_I \leq G_C \\ n_1 C_R \left[1 - \left(\frac{G_C}{G_I} \right)^{n_2} \right] & , \quad G_I > G_C \end{cases} \quad (10)$$

where C_R is the Rayleigh wave speed, G_c is the critical strain energy release rate for microcrack growth, and G_I is the applied strain energy release rate. The n_1 is used to limit the microcrack growth rate. For a given value of G_I , small positive values ($\ll 1$) of n_2 will tend to reduce the microcrack growth rate, while large positive values (> 1) of n_2 will increase the microcrack growth rate. Different crack extension rates are assumed for tensile and compressive loading conditions. As a result, the microcrack extension model has four parameters: n_1^- , n_2^- , n_1^+ , and n_2^+ , where n_1^- and n_2^- are used for crack sliding, and n_1^+ and n_2^+ are used for crack opening. The ceramic is assumed to pulverize under compression when γ reaches a critical value of 0.75, as described in Ref. [1]. The strength of the post-fractured ceramic is described by:

$$Y = \alpha + \beta P \quad (11)$$

where α and β are the model constants. In the present work, values for these two post-fracture model constants are arbitrarily assumed to be equal to 0 and 1, respectively. In a later section, the effects of β on the computed stress profiles are presented to justify this assumption. Since these two constants describe the strength of the fractured ceramic, they influence the depth of penetration (DOP) of a projectile into a ceramic target. Therefore, the use of DOP data is necessary in the determination of the post-fracture model constants.

2.4. Plate impact experiment

Plate impact tests provide a loading path that is very different from conventional split Hopkinson bar (SHB) tests. The deformation is that of one-dimensional strain, and the mean stress is generally very high compared to that in the SHB tests under one-dimensional stress states. Strain rates are $10^5/s$ or higher. The material undergoes compression followed by tension. In general, plate impact experiments are essential for calibrating and validating high strain rate material models that aspire to general applicability.

Figure 1 shows typical velocity profiles that correspond to different levels of spallation. The challenging part of modeling the impact behavior of ceramics is in the model's ability to reproduce these profiles at various velocity levels using the same set of model parameters. A particular level of spall occurs according to the impact velocity level for a given flyer-target configuration. The thickness and material of the flyer plate affects the pulse duration. Initially, through trial and error, model constants can be determined by matching the computed stress and/or velocity profiles with experimentally measured profiles. However, this preliminary determination may not assume the generality

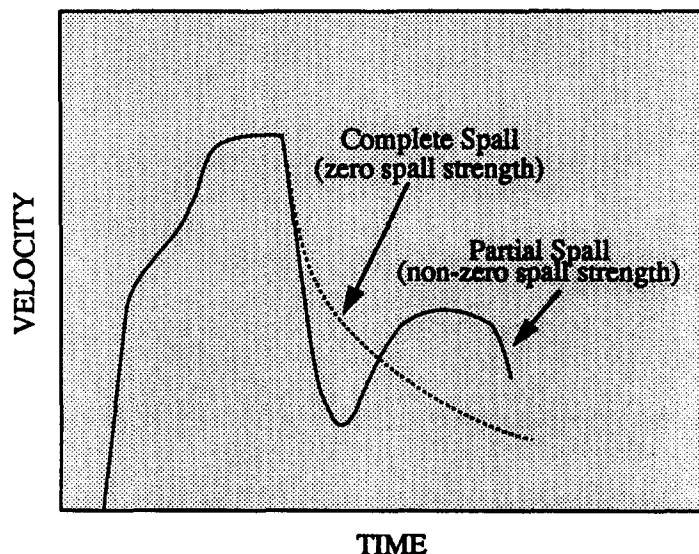


Fig. 1. A sketch of typical velocity profiles indicating various levels of spalls.

of the model constants. Some constants may be further improved by calibrating them against data from other experimental configurations. Rajendran [1] exercised this approach for AD85 ceramic and determined model constants that were configuration independent.

The plate impact tests considered in the present study were conducted by Kipp and Grady [3] to determine:

- (1) Hugoniot Elastic Limit;
- (2) loading and unloading paths from the free surface velocity history; and
- (3) spall threshold of SiC, B₄C, and TiB₂.

A detailed discussion on plate impact experiments is provided in Ref. [5]. The model parameters determination scheme fully utilized the plate impact test data of Kipp and Grady for SiC, B₄C, and TiB₂.

3. RESULTS AND ANALYSES

Recently, Grove [15] implemented the ceramic model in the 1991 version of the EPIC code [16]. This modified version of EPIC was subsequently used to determine the ceramic model constants for SiC, B₄C, and TiB₂ by matching the VISAR data from the plate impact experiments of Kipp and Grady [3]. Two impact experiments were performed for each of the three ceramics, one at a lower level of about 1.5 km/s, and the other at a higher level of about 2.1 to 2.2 km/s. Table 1 provides the details of these experiments. Preliminary ceramic model constants were determined using the lower velocity data. In other words, only tests 1, 3, and 5 were employed in the model constants calibration scheme. Later, the VISAR results of the higher velocity tests (2, 4, and 6) were predicted through EPIC simulations by employing the values determined from the low velocity tests. The measured shock stresses (maximum axial stresses) were two to four times the Hugoniot elastic limit of the ceramics.

The following subsections describe the sensitivity studies that were performed to evaluate the effects of mesh, time step and model parameter variation on the ceramic model results. In addition, preliminary model constants are presented for SiC, B₄C, and TiB₂, along with discussions of the shock responses of these three ceramics, based on the plate impact simulation data. In all the simulations, the ceramic strength and stiffness were assumed to degrade due to microcracking.

3.1. Mesh and time step sensitivity study

Since the governing constitutive equations are coupled nonlinear equations, a stable and accurate solution demands a robust numerical scheme which will assure not only convergence of the solution, but also yield mesh and time step independent solutions. Grove [15] used a diagonally implicit Runge–Kutta scheme in the implementation of the model into the EPIC code. The one-dimensional strain option in the EPIC code was used to simulate the plate impact configuration. To investigate the effects of time step and mesh size on the numerical results, two different time steps and meshes were considered. A baseline velocity profile for a 0.2 mm mesh was obtained from a plate impact simulation of test 1 (see Table 1). The model parameters used to generate this baseline

Table 1. Kipp and Grady [3]: Plate impact experimental details

Test No.	Material	Impact velocity (m/s)	Flyer thickness (mm)	Target thickness (mm)
1	SiC	1542	3.987	8.933
2	SiC	2100	3.995	8.940
3	B ₄ C	1546	3.920	9.044
4	B ₄ C	2210	3.917	9.033
5	TiB ₂	1515	3.972	10.804
6	TiB ₂	2113	3.337	10.747

profile were:

$$\begin{aligned}
 N_0^* &= 10^9; \\
 a_0 &= 0.0005 \text{ mm}; \\
 K_{IC} &= 4 \text{ MPa}\sqrt{\text{m}}; \\
 \mu &= 0.1; \\
 n_1^- &= 0.1; \text{ and} \\
 n_2^- &= n_1^+ = n_2^+ = 1.0.
 \end{aligned}$$

To investigate the mesh size effect, a simulation with a 0.1 mm mesh was performed. The results were almost identical. The time step effect was also studied by performing two simulations with maximum allowable time steps of 0.01 μs and 0.001 μs . The resulting velocity–time histories were almost identical, confirming a minimum influence of the time step on the numerical results.

3.2. Sensitivity study on model constants

There are eight constants in the ceramic model to describe the microcracking behavior: N_0^* , a_0 , μ , n_1^- , n_2^- , n_1^+ , n_2^+ , K_{IC} . In the present modeling efforts, the crack growth factor n_1^+ and the crack growth indices n_2^+ and n_2^- are assumed to be equal to 1. Under compressive loading (positive pressure), the best value for n_1^- can be determined by matching the computed stress or velocity profile with the plate impact experimental data. Direct measurements of the microcrack parameters a_0 , N_0^* , and μ (dynamic coefficient of friction) are extremely difficult to make. The estimation of realistic values for these constants requires microstructural characterization of the virgin ceramic material through both non-destructive and destructive test techniques. In this study, due to lack of experimental measurements, the initial microcrack size was assumed to be equal to a fraction of the average grain size, and the number of flaws was estimated through numerical simulations of the plate impact experiments.

To understand the significance of several of the model constants on the shape and amplitude of the measured velocity histories, a sensitivity study was conducted. In effect, there are only four adjustable constants to describe the microcracking behavior: N_0^* , a_0 , μ , and n_1^- . Therefore, the main idea behind the sensitivity study was to identify a range of values for these four model parameters and isolate the effects of any one parameter or a combination of parameters on certain portions of the stress/velocity history. This was accomplished through EPIC simulations of the plate impact configuration of test 1 (see Table 1). Based on this sensitivity analysis, it may then be possible to develop a standard methodology to estimate appropriate values for the model constants.

3.3. Number of flaws, N_0^*

Three simulations were considered using the values of 10^{11} , 10^9 (baseline case), and 10^7 for N_0^* . The corresponding results are presented in Fig. 2. The value of 10^7 did not produce complete spall fracture. The ceramic retained some of its spall strength, indicated by the dashed curve beyond point ‘S’. The intermediate value of 10^9 produced minimal compressive cracking followed by complete spall due to tensile cracking. The high value of 10^{11} caused excessive damage under compression. This resulted in degradation of the shear modulus of the ceramic, significantly affecting the computed velocity profile between points ‘A’ and ‘C’ (see Fig. 2). However, the spall signal (between points ‘D’ and ‘E’) is very similar to that of the velocity profile for $N_0^* = 10^9$. Based on these simulations, 10^9 seems to be a reasonable value for N_0^* in order to cause spall without excessive compressive damage during the initial shock.

To illustrate the reason for the difference between the velocity profiles for N_0^* values of 10^9 and 10^{11} , Fig. 3 compares the time histories of pressure, damage, and axial stress for a target element very close to the impact plane for $N_0^* = 10^{11}$. In this figure, the pressure and stress are normalized with respect to σ_{HEL} (= 15 GPa) so that the damage history can be presented in the same plot. For 10^9 , the damage level remained low during the initial compressive shock pulse, whereas for 10^{11} , the compressive damage reached a value of 1 (pulverization) at about 0.25 μs . The normalized pressure level continues to remain at the same level beyond the point of pulverization. Since the bulk modulus does not

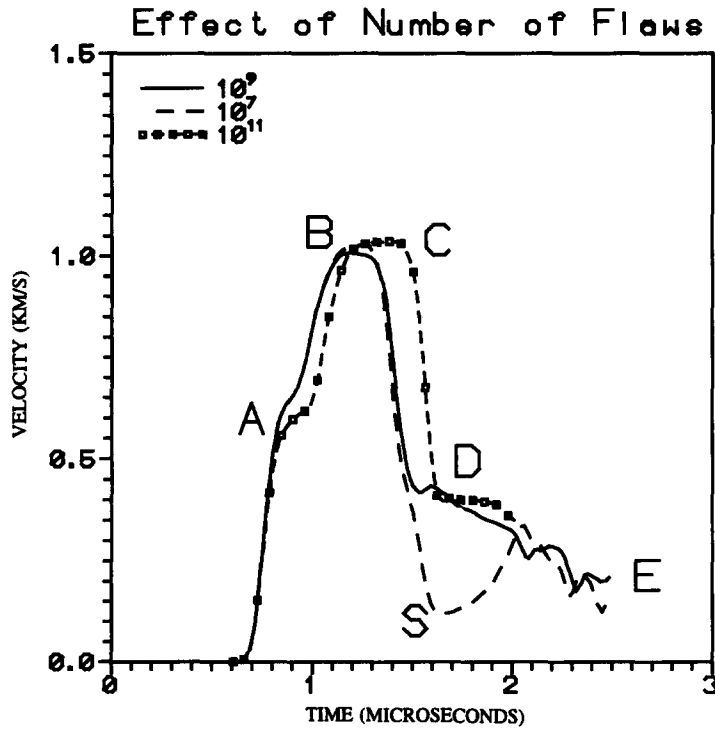


Fig. 2. The effect of the number of flaws on the computed velocity profile.

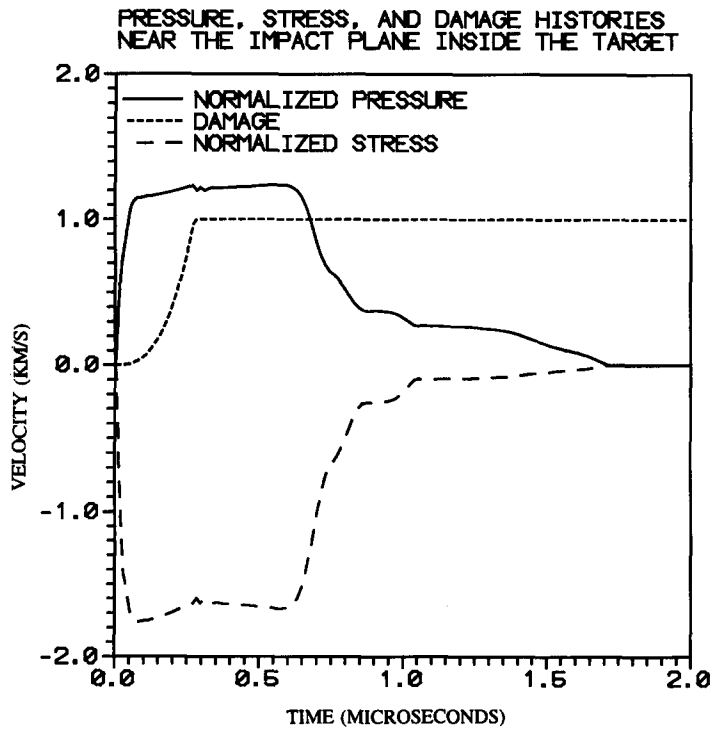


Fig. 3. The time histories of pressure, stress, and damage in an element near the impact plane.

degrade under compressive pressure, especially when all the three principal stresses are compressive, the shock pressure level does not change.

Due to absence of dilatation under high confinement pressure, the density of the confined granular ceramic remains the same as that of the intact ceramic. If one of the three principal stresses becomes tensile while the pressure remains under compression, crack opening could occur, causing dilatation.

Under such loading conditions the model will degrade the bulk modulus. This is not the case for an element that is close to the impact plane as can be seen from the normalized stress profile (dashed line) in Fig. 3. The axial stress remains compressive, eliminating any bulk modulus degradation possibilities.

3.4. Initial microcrack size, a_0

To investigate the effect of microcrack size on ceramic fracture, three simulations with a_0 values of 0.1 micron (μm), 0.2 μm , and 1.0 μm were considered. In these simulations, μ was 0.1 and N_0^* was 10^9 . The velocity-time histories for these three values are compared in Fig. 4. No microcracking occurred for values of a_0 less than or equal to 0.1 μm . An additional simulation with $a_0 = 0$ produced a velocity profile identical to that of the 0.1 μm simulation. Partial spall occurred with $a_0 = 0.2 \mu\text{m}$, and initial crack sizes greater than 0.35 μm induced complete spall in the target. Initial microcrack sizes between 0.1 and 0.35 μm did not influence the loading wave portion of the profile between points 'A' and 'C' as well as the elastic release between points 'C' and 'S'. These critical values of a_0 will vary with the selection of different values for the other two microcrack parameters, μ and N_0^* .

3.5. Coefficient of friction, μ

Figure 5 shows the effect of μ on the velocity profile for $n_1^- = 0.2$. The main influence of this parameter is to increase or decrease the applied shear stress level required to satisfy the Griffith criterion under compressive pressure. Several simulations were performed to investigate this influence. The value for this parameter is closely tied to the values chosen for some of the other model constants, especially the compressive crack growth factor n_1^- . For instance, the effect of μ was insignificant for $n_1^- = 0.1$, whereas the effect became significant for $n_1^- = 0.2$.

In the simulations, lower values of μ tended to cause premature microcracking while the shock amplitude was still increasing during the 'plastic' wave ramp between points 'B' and 'C'. Since the compressive microcracking occurred well above the threshold level of 'complete spall (under tension)', the influence of μ on the spall signal was negligible. This study suggests that a minimum value which will not cause any premature compressive damage shall be assigned to μ . In fact, this minimum value

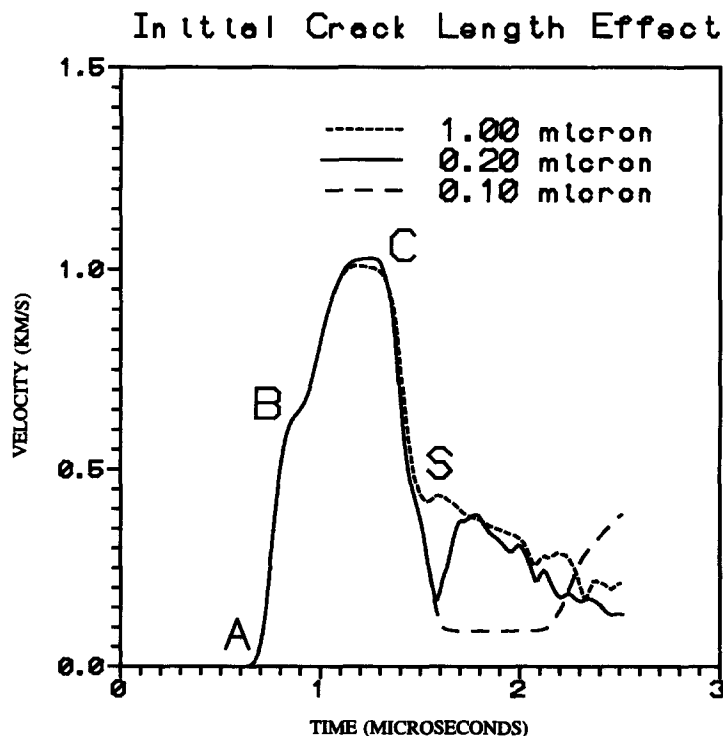


Fig. 4. The effect of initial crack size on the computed velocity profile.

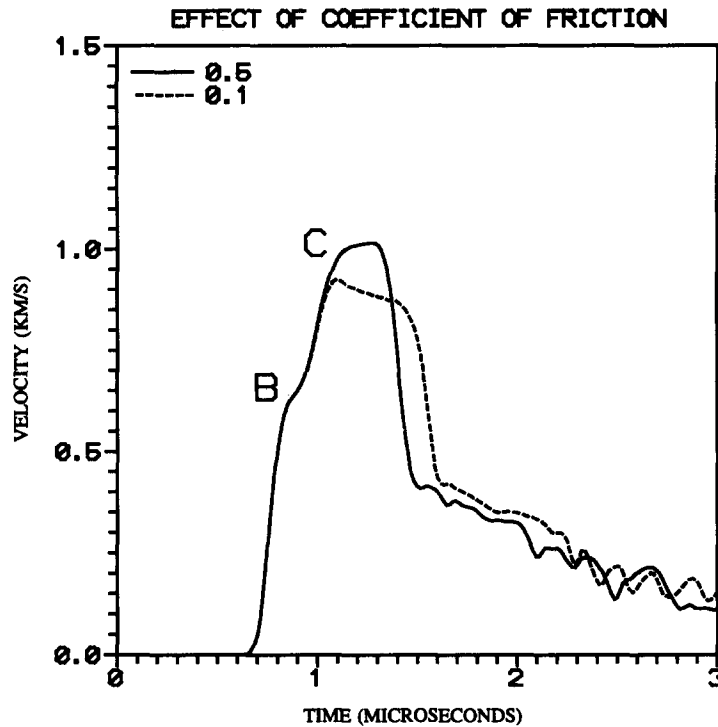


Fig. 5. The effect of coefficient of friction on the computed velocity profile.

will allow the independent determination of the other constants. When calibrating the model constants for SiC, B₄C, and TiB₂, a value of 0.1 was assumed for μ .

3.6. Compressive crack growth factor, n_1^-

This model constant limits the microcrack growth rate (see Eqn 10) under compression to $n_1^- C_R$. When the Griffith criterion is satisfied for a given stress state, the time dependent microcrack extension controls the rate at which the elastic moduli are degraded. This degradation affects the shock wave speed and this, in turn, affects the pulse duration. Experimentally measured values are available for the limiting dynamic crack propagation velocity under crack opening (mode I). However, such measurements are not available for dynamic crack propagation under mode II (crack sliding under shear). The n_1^- effect on the computed velocity profile is shown in Fig. 6.

Values of n_1^- lower than 0.1 did not introduce any further change in the profile. Increasing n_1^- to 0.2 widened the pulse width due to elastic moduli degradation. The shock amplitude diminished as the compressive microcracking increased with increasing n_1^- . The spall rebound portion of the velocity profile was not significantly affected by the n_1^- variations. This is because the crack damage degradation of the elastic properties during compression exceeds the threshold to cause complete spall immediately upon the arrival of the tensile stress wave.

3.7. Compressive crack growth index, n_2^-

To verify the effect of n_2^- on the velocity profile, several simulations were performed. The results showed that the computed profile was unaffected by n_2^- . Since the ratio between G_c and G_1 is very small at impact velocities above 1 km/s, varying this index between 0.001 and 1 did not alter the ceramic response. However, two additional simulations at a lower velocity also produced very similar wave profiles. Grove *et al.* [17] found that this index influenced the computed stress histories in a ceramic rod due to an impact by a similar rod at low velocity. In their study, the states of stress and strain at the gauge location were one-dimensional (uniaxial) stress and three-dimensional strain, respectively, whereas in the plate impact configuration, the stress state is three-dimensional and the strain state is one dimensional.

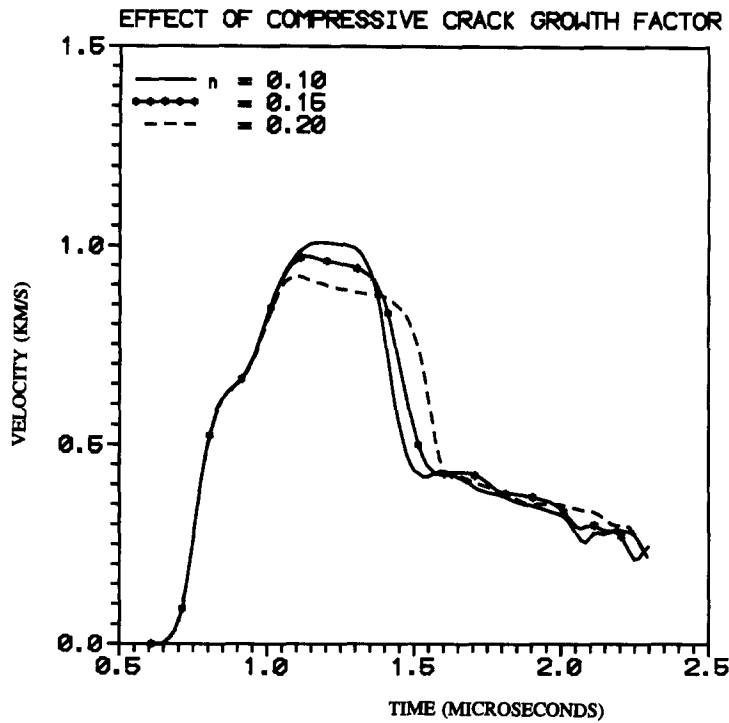


Fig. 6. The effect of compressive crack growth factor on the calculated velocity profile.

3.8. Tensile crack growth factor, n_1^+

Ceramics are very weak under tensile loading. The fracture toughness of a ceramic is very low compared to metals. Upon high velocity impact, compressive shock loading initiates damage in the ceramic. When the tensile wave arrives at locations where the ceramic has been partially damaged due to the initial compressive shock, it induces additional damage leading to complete spall. The tensile crack growth factor limits the microcrack growth rate (see Eqn 10) under tension to $n_1^+ C_R$. The computed velocity profiles for n_1^+ equal to 0.2, 0.3, and 1.0 are shown in Fig. 7.

The crack density levels increase with increasing values of n_1^+ . Since the degradation of spall strength is not complete for lower values of n_1^+ , the calculated profiles showed pull back signals (spall rebounds), indicating nonzero spall strength. The value of 1 caused complete spall in the ceramic target as can be seen from the velocity profile between points 'E' and 'F' (solid curve). By comparing these simulations with an experimental profile, a suitable value for n_1^+ can be chosen to model the impact behavior of any ceramic. Experimental measurements on a single crack opening under dynamic tensile loading conditions suggest that the Rayleigh wave speed is the limiting crack propagation speed. Therefore, in the present analysis, n_1^+ was assumed to be equal to 1 for all three ceramics, eliminating the need for determining this constant from the plate impact experiments.

3.9. Tensile crack growth index, n_2^+

This parameter appears as an exponent in the damage evolution law of Eqn 10. The ratio of critical strain energy release rate (with respect to crack extension), G_c , and applied strain energy release rate, G_I , is modified through n_2^+ . The ratio is equal to 1 when $G_c = G_I$. Microcrack growth occurs when this ratio is below 1. As soon as the Griffith criterion is satisfied and the ratio is still close to 1, this index begins to influence the microcracking process. However, the effect on the computed velocity profile is significant only for extremely low values of the index, as shown in Fig. 8.

A value of 0.01 suppressed spall fracture, though the Griffith criterion was satisfied. The larger values of 0.1 and 1.0 produced complete spall; the corresponding profiles were similar. Apparently, to allow complete spall, a value between 0.1 and 1 should be chosen for the tensile crack growth index n_2^+ . For simplicity, a value of 1 was chosen to model the three ceramics.

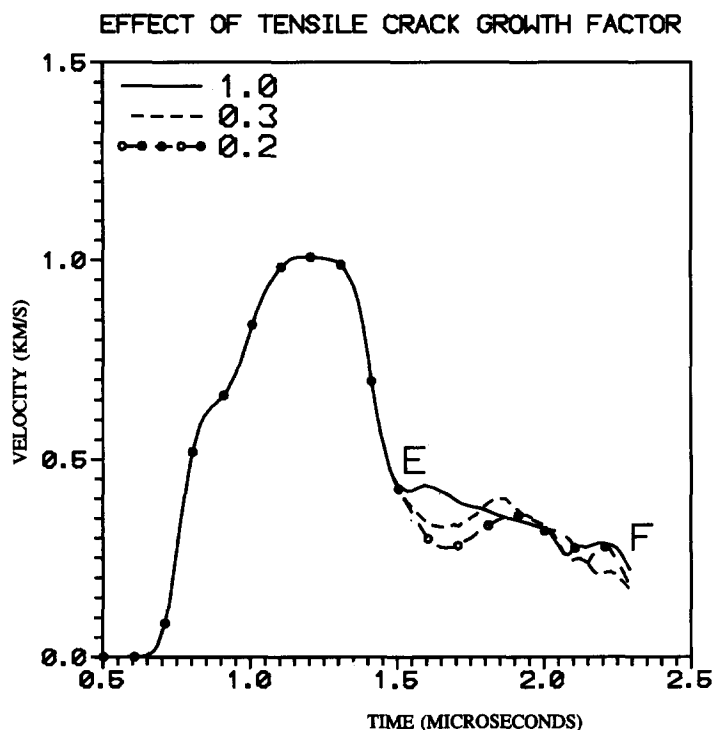


Fig. 7. The effect of tensile crack growth factor on the computed velocity profile.

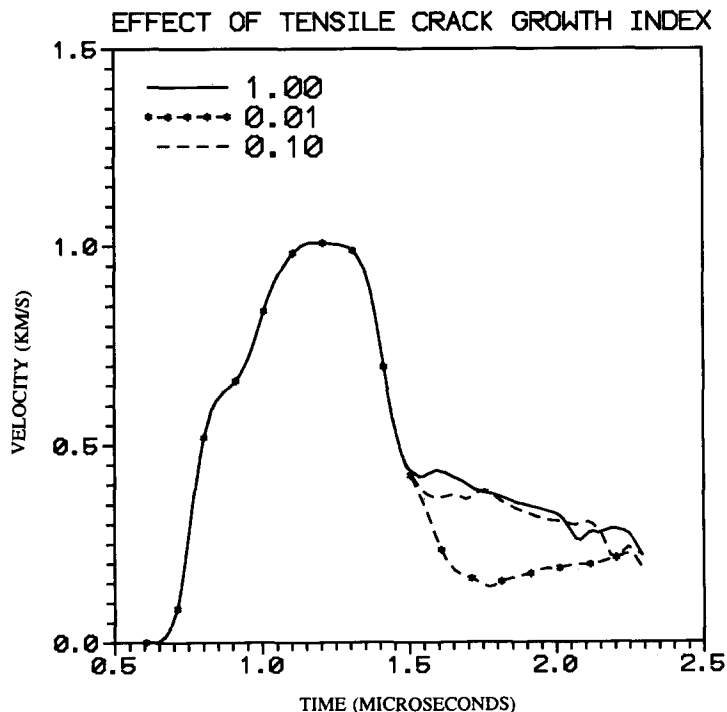


Fig. 8. The effect of tensile crack growth index on the computed velocity profile.

3.10. Fracture toughness, K_{IC}

The ceramic model does not contain a microflaw nucleation model. Numerous flaws are assumed to exist in the virgin ceramic material. These flaws are activated when the stress state satisfies the Griffith criterion for an initial flaw of size a_0 . Values of K_{IC} between 1 and 20 $\text{MPa}\sqrt{\text{m}}$ did not show any effect on the velocity history. For several ceramics, Suresh *et al.* [18] tabulated the values of

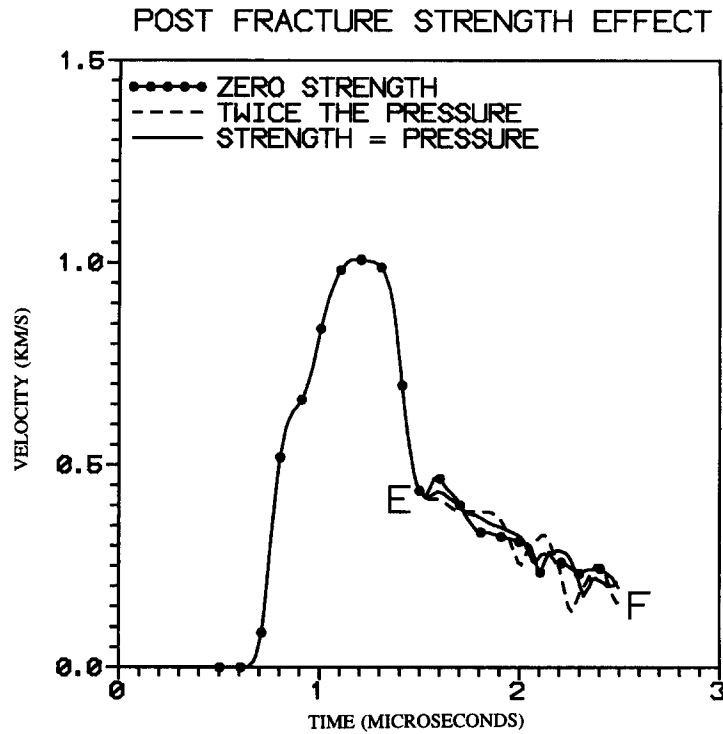


Fig. 9. The effect of post-fracture strength model parameter β on the computed velocity profile.

dynamic fracture toughness (K_{1d}) from experimental measurements. The measured K_{1d} values were about 10–40% higher than the corresponding K_{1c} values. However, the calculated applied strain energy release rates in high velocity impact problems, such as projectile penetration into ceramic targets and flyer plate impact, are several orders of magnitude higher than the critical strain energy release rate based on dynamic fracture toughness values. Therefore, the readily available static fracture toughness values from handbooks are employed in the model.

3.11. Post-fracture strength parameter, β

The plate impact experimental configuration seems to be insensitive to this parameter. The simulations with three different values for β showed minimal effect on the computed velocity profiles as can be seen in Fig. 9. In the post-fracture strength model (Eqn 11), the strength of the pulverized ceramic is directly proportional to the applied pressure when $\alpha=0$. The strength is zero for $\beta=0$, twice the pressure for $\beta=2$, and equal to the pressure from $\beta=1$. In the figure, the average spall signal between points 'E' and 'F' is almost the same for the three values of β . It appears that the calibration of this parameter should be based on some other type of impact test configuration, such as the configuration in which a rod penetrates into a ceramic plate. The computed stress profiles for $\alpha=1, 5$, and 10 kbars did not influence the results either. Therefore, in the model constant calibration scheme, α was set to 0 and β was set to 1 for the three ceramics.

4. MODELING OF SiC, B₄C, AND TiB₂

As Table 1 indicates, Kipp and Grady [3] performed plate impact tests at two different velocities on each of three ceramics: silicon carbide (SiC), boron carbide (B₄C), and titanium diboride (TiB₂). In each test, a laser velocity interferometer (VISAR) was used to record the target plate's back surface velocity history. These tests were all simulated using the 1991 version of the EPIC code [16], modified to include the ceramic model. For each ceramic material, preliminary model constants were calibrated by matching the measured velocity profile from the lower velocity test. These constants were then employed to predict the VISAR data from the higher velocity test. The preliminary ceramic model

Table 2. The ceramic model constants

Model constants	SiC	B ₄ C	TiB ₂
f_0 (porosity content)	0.0	0.03	0.0
K_{IC} (MPa \sqrt{m}) (fracture toughness)	4	2	7
μ (coefficient of friction)	0.1	0.1	0.1
N_0^* (m ⁻³) (number of flaws)	1×10^9	5×10^9	1×10^9
n_1^-	0.1	0.1	0.15
a_0 (microns) (initial crack size)	0.5	0.5	2.0

Table 3. Equation of state and strength constants

Other constants	SiC	B ₄ C	TiB ₂
Density (kg/m ³)	3177	2516	4452
β_1 (GPa)	204	233	230
β_2 (GPa)	204	50	930
β_3 (GPa)	0	0	-1310
Γ	1	1	1
Y_{HEL} (GPa)	11.5	12.5	12.0
C_3	0.01	0.01	0.01
G (GPa)	187	199	237

constants are given in Table 2. The strength and equation of state parameters given in Table 3 were employed by Johnson and Holmquist [5] in their modeling of Kipp and Grady's experimental data.

Steinberg [4], Johnson and Holmquist [5], and Addessio and Johnson [6] successfully reproduced the measured velocity profiles of Kipp and Grady [3]. In general, the shock behavior of SiC is relatively straightforward compared to B₄C and TiB₂. These two high strength ceramics exhibited heterogeneous deformations. The strain rate and pressure hardening behaviors in these ceramics did not follow the metal behavior.

4.1. Silicon carbide (SiC)

The shock portion of the wave profile for SiC resembled a typical wave profile of a rate sensitive metal. In fact, Kipp and Grady [3] successfully analyzed the low and high velocity tests on silicon carbide using a strain hardening model applicable for metals. The absence of large release wave dispersion in SiC enabled the successful use of a simple metal-based model. The experimental data did not reveal any phase transformation in SiC up to about 36 GPa. The HEL kink appeared at about 15 GPa in both tests.

Figure 10 compares the ceramic model generated velocity versus time plot with Kipp and Grady's data for SiC at an impact velocity of 1542 m/s. The model reproduced all the salient features of the data. As a next step, the higher velocity (2100 m/s) plate impact experiment was simulated using the same set of values for the model constants. The simulation-predicted velocity profile matched the data extremely well as shown in Fig. 11. The ceramic model reproduced all the salient features of the experimental data.

The simulated stress-strain path in the center of the SiC target is plotted in Fig. 12. In this figure, the compressive stress and compressive pressure are plotted as positive quantities. The computed HEL is at about 18 GPa. The experimental value was about 15 GPa. The increased value in the computation is due to the strain rate dependent term in Eqn 7. It is possible to lower the value of C_1 and adjust the value of C_3 to match the computed stress at HEL with the data. However, for the sake of simplicity in the model constant determination scheme, the value of Y that corresponds to the stress at HEL (see Eqn 8) is assigned to C_1 .

Therefore, the transition from elastic to plastic deformation is controlled by the strain rate dependent strength. A value of 11.5 GPa was employed in the SiC simulations. Though C_1 was chosen to be equal to this value, the high $\dot{\epsilon}$ ($> 10^4/s$) slightly increased the computed value of Y . This in turn caused a slight increase in the computed σ_{HEL} . Kipp and Grady obtained a value of about 16 GPa in

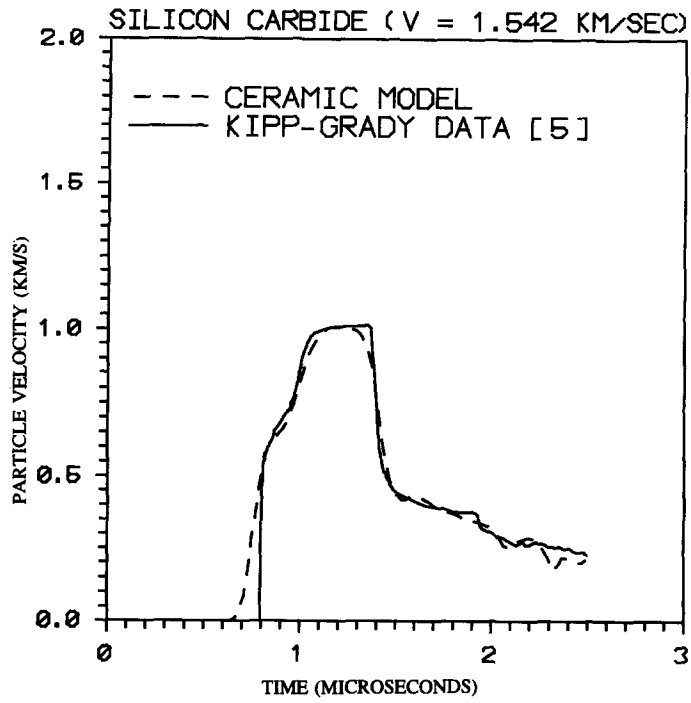


Fig. 10. A comparison between model generated velocity profile with the Kipp and Grady plate impact experimental data at impact velocity 1542 m/s for silicon carbide.

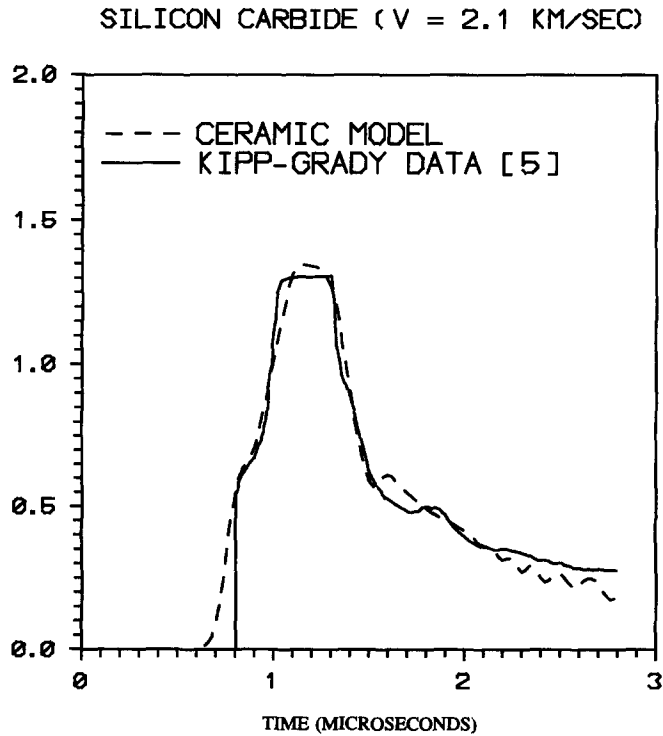


Fig. 11. A comparison between model generated velocity profile with the Kipp and Grady plate impact experimental data at impact velocity 2100 m/s for silicon carbide.

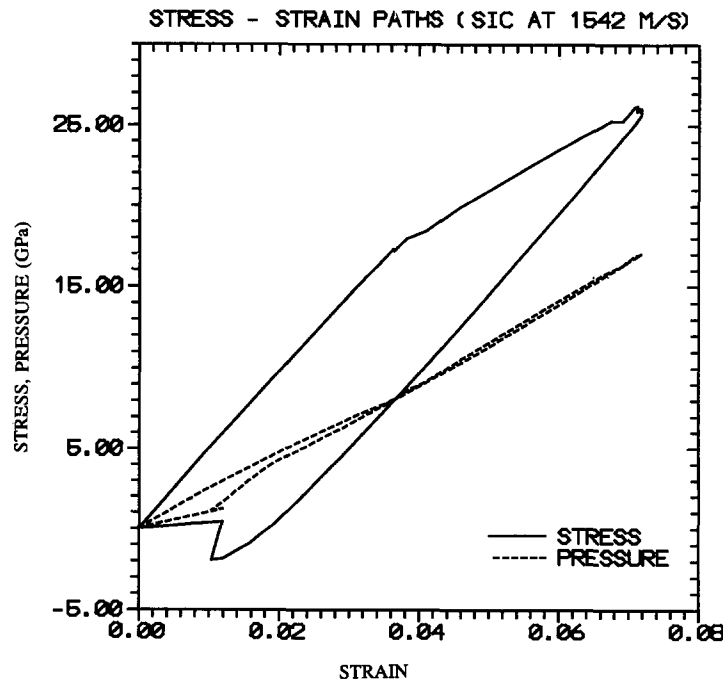


Fig. 12. The stress-strain path (under one-dimensional strain) in the midplane of a silicon carbide target. (The dotted line is the computed hydrostat).

their computational analysis. The maximum stress amplitude in compression reached about 26 GPa and elastically unloaded past the hydrostat (the dotted line curve).

At about 0.02 strain, the stress became tensile and reached a tensile maximum of about 2 GPa. The ceramic model reduced the stress amplitude in tension due to microcracking. The ability to control the tensile stress amplitude is an important feature of the model. The degradation of the tensile strength due to microcracking was a continuous (not instantaneous) process and therefore, the stress relaxation occurred continually until the microcrack density reached a critical value of 9/16, as determined by Budiansky and O'Connell [19] for tensile pressure loading conditions.

The pressure versus volumetric strain plot showed different loading and unloading paths. Since the model degraded the bulk modulus according to microcracking under tensile loading, the unloading path between the strains of 0.02 and 0 differed from the loading path. The slight difference between the loading and unloading paths at strains above 0.04 was due to mild microcracking under compression. As mentioned earlier, crack opening is possible under compressive pressure when one of the principal stresses is positive (tension).

The time histories of damage and axial stress at the midpoint of the ceramic target are plotted in Fig. 13. For comparison purposes, the stress is normalized by σ_{HEL} ($= 15 \text{ GPa}$). Microcracking began at point 'A' under compressive loading and reached a maximum of about 0.2 at point 'B' in the figure. At this point, the stress (dotted line) became tensile (negative in the figure) and the damage level abruptly increased to 1. According to the model, the ceramic material at the midpoint of the target failed due to tensile cracking and could no longer support any tensile stress.

The maximum amplitude of the tensile stress is controlled by the degradation of shear and bulk moduli under tensile loading. When the crack density reaches a critical value of 9/16 in the Budiansky and O'Connell [18] relationship, the damage reaches 1 (point 'C' in Fig. 13) and both moduli become zero. When this occurs in the simulation, the element is assumed to have failed under tension, and the stresses and pressure are set to 0. However, an element that has failed in tension can still sustain compressive stresses.

4.2. Boron carbide (B_4C)

Figure 14 compares the computed velocity profile with the experimental measurement for boron carbide at 1546 m/s. Kipp and Grady [3] and Steinberg [4] provided some explanations for the

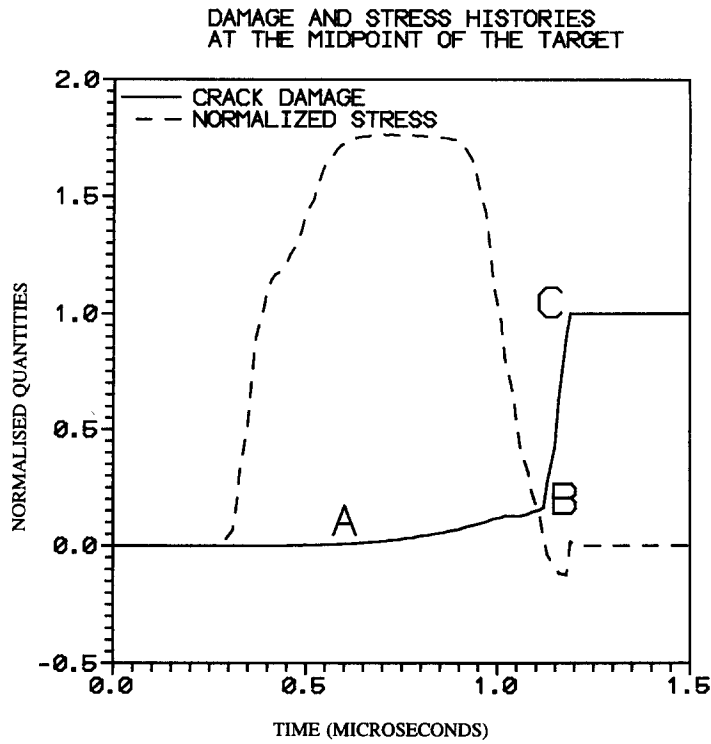


Fig. 13. The computed damage and stress histories at a midsection of the silicon carbide target. The axial stress is normalized by $\sigma_{HEL} = 15$ GPa.

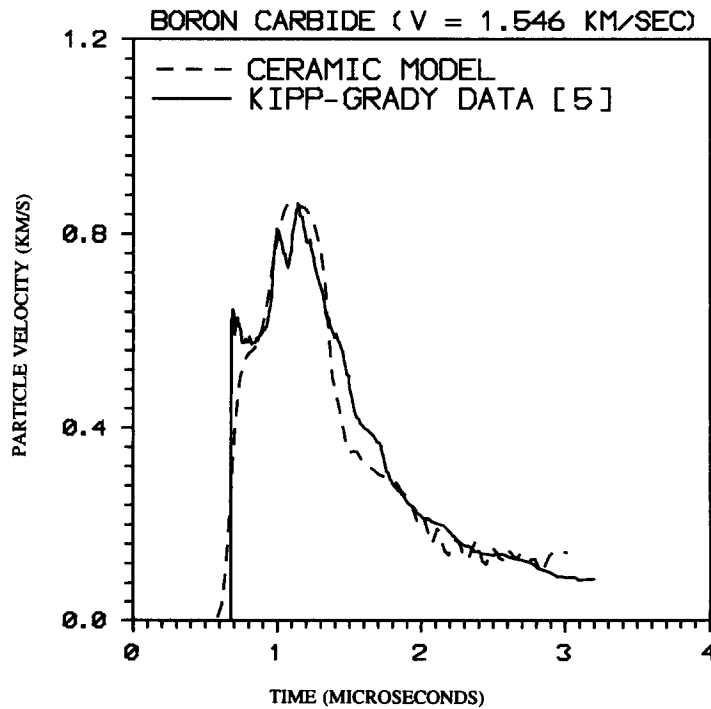


Fig. 14. Comparison between model and Kipp and Grady [3] data for a boron carbide target (test 3 in Table 1).

unusual behavior of this material under high velocity impact loading. According to Kipp and Grady, the sporadic nature of the wave profile at the HEL can be attributed in part to a heterogeneous failure or faulting mechanism during the initial shock loading.

The plateau at the HEL also means a slower shock speed compared to the elastic wave speed. In the present study, an attempt was made to model the overall (average) response of B_4C . To describe the

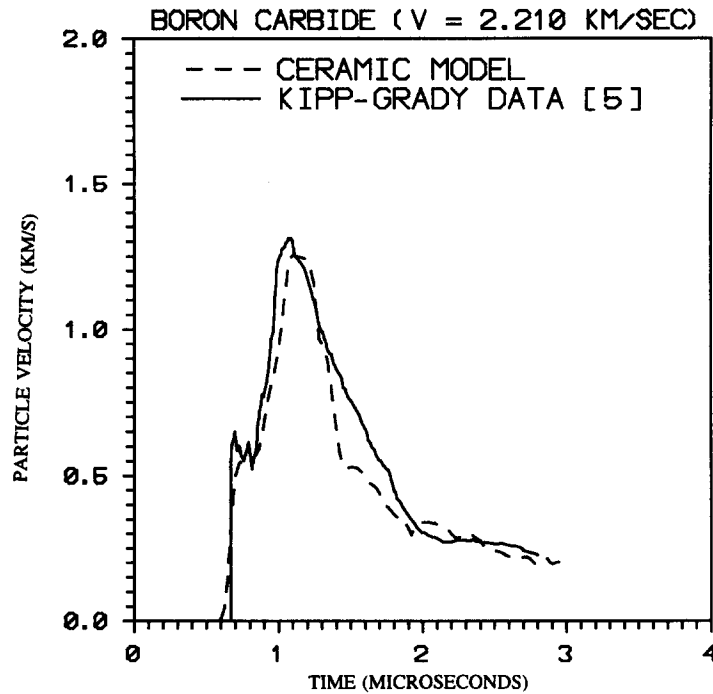


Fig. 15. Comparison between model and Kipp and Grady [3] data for a boron carbide target (test 4 in Table 1).

complex behavior of B_4C , preliminary ceramic model constants (see Table 2) were obtained by matching the computed velocity history with the data from test 3 (see Table 1). The corresponding comparison between the model and the data is given in Fig. 14.

The measured velocity history from the higher velocity (2210 m/s) plate impact experiment was then predicted using the same set of constants. Figure 15 compares the computed velocity history with the measured data from test 4. While the model predicted the experimental data very well, it was unable to capture the entire dispersive nature of the unloading portion of the velocity profile. However, damage evolution due to time dependent microcracking processes led to the degradation of the elastic moduli, and this degradation resulted in some sort of dispersion of the unloading wave. In general, the ceramic model's ability to reproduce the data from the low and high velocity tests on B_4C is quite impressive.

4.3. Titanium diboride (TiB_2)

The measured velocity histories from the two plate impact experiments on TiB_2 , one at 1515 m/s and the other at 2113 m/s, are compared in Fig. 16. The material typically revealed two breaks in the loading wave portion of the measured profiles. In the present effort, no attempt was made to model the two breaks. The initial compressive loading in the lower velocity experiment (test 5) was very dispersive with a large rise time compared to the higher velocity test no. 6.

The release wave from the flyer arrived sooner in the higher velocity case. This shorter pulse duration can be partially attributed to the differences in flyer plate thicknesses (3.972 mm in test 5 vs. 3.337 mm in test 6). In addition, the computational analysis of Kipp and Grady indicates shock wave formation above 13.7 GPa in TiB_2 . This would lead to a faster shock wave speed in the higher velocity test as opposed to the dispersive loading wave in the lower velocity test, which could help explain the shorter pulse duration.

The preliminary ceramic model constants for TiB_2 (see Table 2) were determined by matching the computed velocity history with the data from test 5. Figure 17 compares the computed velocity profile with the data. As the figure indicates, the ceramic model reproduced all the salient features of the measured velocity profile, including the dispersive nature of the loading as well as the unloading waves.

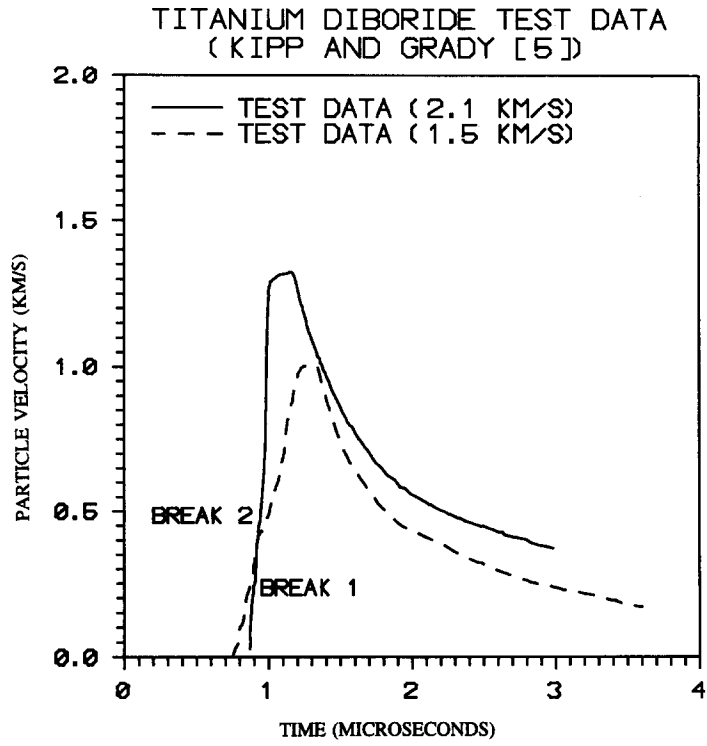


Fig. 16. The measured velocity profiles from the two plate experiments of Kipp and Grady [3] on titanium diboride targets are compared.

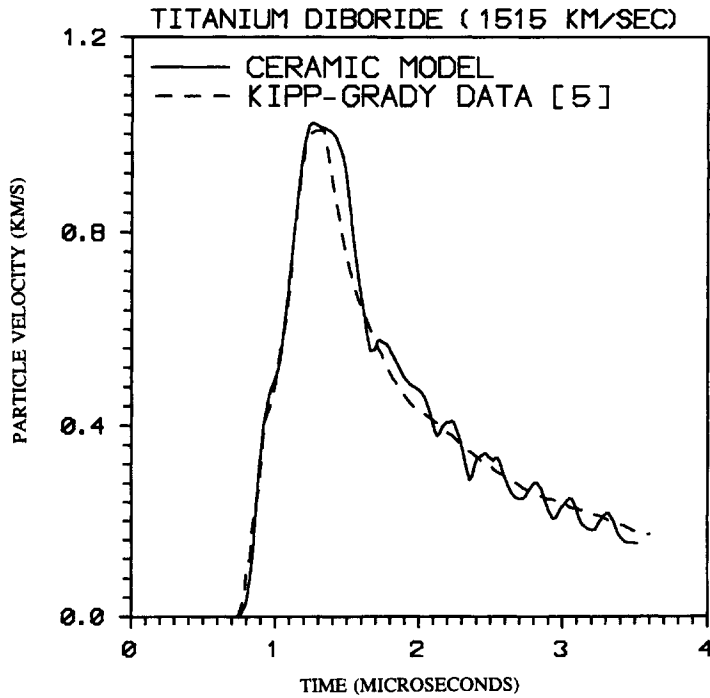


Fig. 17. A comparison between model generated velocity profile with the Kipp and Grady plate impact experimental data at impact velocity 1515 m/s for TiB_2 .

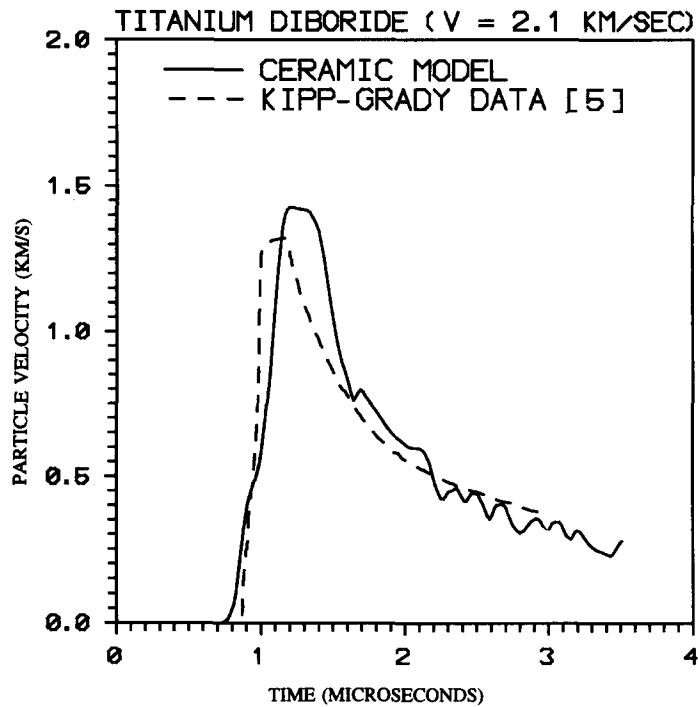


Fig. 18. A comparison between model predicted velocity profile with the Kipp and Grady plate impact experimental data at impact velocity 2100 m/s for TiB_2 .

The velocity profile from the higher velocity experiment (test 6) was then predicted using the set of constants that had been calibrated based on the lower velocity experiment (test 5). Figure 18 compares this model prediction with the VISAR data. The model showed more dispersion of the loading wave than indicated by the experiment. Assuming that TiB_2 shocks up above a shock stress of about 13.7 GPa, the equation of state and constitutive equations were unable to model the high amplitude experimental data. However, a decent matching occurred between the spall portions of the computed and experimental profiles.

5. SUMMARY AND CONCLUSIONS

5.1. Summary

Recently, Rajendran [1, 2] reported the development and application of an advanced ceramic model. This ceramic model was implemented into the 1991 version of the EPIC code by Grove [15] and successfully used to model the impact behavior of three ceramics: SiC , B_4C and TiB_2 .

There are eight microcrack model constants: N_0^* , a_0 , μ , K_{IC} , n_1^- , n_2^- , n_1^+ and n_2^+ . A porous ceramic requires one additional constant, f_0 , which is the initial porosity. The fracture toughness (K_{IC}) value can be taken from fracture mechanics handbooks. Based on a sensitivity study, the coefficient of friction μ is assumed to be equal to 0.1. The tensile crack growth factor n_1^+ , the tensile crack growth index n_2^+ , and the compressive crack growth index n_2^- are assumed to be equal to 1, thus eliminating the requirement for determining these three constants. Therefore, based on these assumptions, the ceramic model effectively required the calibration of only three microcrack constants and one porosity constant for SiC , B_4C , and TiB_2 .

The ceramic model constants can be calibrated by matching the simulated velocity or stress profiles with the measured profiles from a plate impact experiment. For the strength model, C_1 is assumed to be equal to the ceramic's compressive strength at HEL (Y_{HEL}), and the rate sensitivity constant (C_3) is calibrated by matching the shape of the elastic-plastic transition portion of the shock wave (velocity or stress) profile.

In summary, this paper discussed the impact behavior modeling of three ceramics: silicon carbide (SiC), boron carbide (B_4C), and titanium diboride (TiB_2). The main objective of the present work was to determine preliminary ceramic model constants for these materials using the plate impact experimental measurements of Kipp and Grady [3]. Based on the assumed values for μ , n_1^+ , n_2^+ , and n_2^- mentioned above, the remaining constants (N_0^* , a_0 , n_1^- , f_0 , and C_3) were adjusted to give the best agreement with the data from the lower velocity plate impact tests. Then, using the calibrated constants, the ceramic model was used to predict the velocity profiles from the higher velocity tests. In general, the model successfully demonstrated its ability to reproduce the experimental data for a range of impact velocities.

5.2. Conclusions

Deformation in ceramic materials due to impact loading consists of elastic, plastic, and microcracking components. It is not experimentally possible to isolate these deformations through any direct measurements. With lack of recovery techniques to examine the post-impacted ceramic targets after high velocity impact, we can only make speculative assumptions concerning the various deformation and fracture processes.

With the aid of advanced ceramic models, computational analyses of impact experiments will indeed help us evaluate the various possible deformation and fracture modes in ceramic materials. So far the experimentalists have produced accurate velocity and stress measurements, high speed photographs, and X-ray radiographs. Interpretation and validation of these valuable measurements demand detailed computational/analytical modeling of the impact experiments. Such modeling efforts will eventually lead to a greater understanding of the impact behavior of ceramics.

In order to increase our confidence in using sophisticated ceramic models as predictive tools in armor/anti-armor applications, the generality of the model parameters should be investigated. For this purpose, impact test configurations involving various stress states and velocity regimes should be modeled using the preliminary constants presented in this paper. Though we could successfully predict the high velocity (2.2 km/s) plate impact experiments well using the constants determined from the low velocity (1.5 km/s) one-dimensional experiments, the generality of the model constants requires further validation. However, availability of a preliminary set of model constants for armor ceramics should encourage scientists and engineers to use advanced constitutive models when performing calculations to evaluate armor/anti-armor designs.

In conclusion, this microphysical ceramic model is capable of modeling the impact behavior of the intact ceramic until pulverization occurs. The accurate and realistic description of the confined pulverized ceramic requires improved equation of state and a physically based strength model. In computer code calculations, a simplistic Mohr–Coulomb type strength model (see Eq. 11) is usually employed to describe the powdered ceramic. While this microphysical ceramic model will certainly improve the quality of computational armor/anti-armor design calculations, the absence of an accurate microphysical model for the fractured (pulverized) ceramic unfortunately diminishes the ceramic model's ability to predict the depth of penetration/perforation of projectiles.

REFERENCES

1. A. M. Rajendran, Modeling the impact behavior of AD85 ceramic under multiaxial loading. *Int. J. Impact Engng*, **15**(6), 749–768 (1994).
2. A. M. Rajendran, High strain rate behavior of metals, ceramics, and concrete. Air Force Report WL-TR-92-4006, Wright-Patterson Air Force Base, OH, U.S.A. 45433-6533, April (1992).
3. M. E. Kipp and D. E. Grady, Shock compression and release in high-strength ceramics. Sandia Report SAND89-1461, Sandia National Laboratory, NM 87185, U.S.A. July (1989).
4. D. J. Steinberg, Computer studies of the dynamic strength of ceramics. *Shock Compression of Condensed Matter 1991*. Elsevier Science Publishers B. V., 447–450 (1992).
5. G. Johnson and T. J. Holmquist, A computational constitutive model for brittle materials subjected to large strains, high strain rates, and high pressures. *Shock wave and High Strain Rates Phenomena in Materials* (1992).
6. F. L. Addessio and J. N. Johnson, A constitutive model for the dynamic response of brittle materials. *J. Appl. Phys.*, **67**(7), 3275–3286 (1990).
7. D. A. Mandell and R. Henninger, Evaluation of two ceramic models in the Mesa codes. LANL Report LA-12267, Los Alamos, NM 87545, U.S.A. February (1992).
8. K. S. Holian, S. J. Mosso, D. A. Mandell and R. Henninger, A 3-D computer code for armor/anti-armor applications. Los Alamos national laboratory report LA-UR-91-569, Los Alamos, NM, U.S.A. 87545 (1991).
9. L. G. Margolin, Elastic Moduli of a Cracked Body. *Int. J. Fracture*, **22**, 65–79 (1983).

10. A. M. Rajendran, M. A. Dietsberger and D. J. Grove, A void growth-based failure model to describe spallation. *J. Appl. Phys.*, **65**(4), 1521–1527 (1989).
11. J. N. Johnson, Dynamic fracture and spallation in ductile solids. *J. Appl. Phys.*, **52**(4), 2812–2820 (1981).
12. L. G. Margolin, A generalized Griffith criterion for crack propagation. *Engineering Fracture Mechanics*, **19**(30), 539–543 (1984).
13. J. K. Dienes, Comments on A Generalized Griffith criterion for crack propagation by L. G. Margolin: a technical note. *Eng. Fracture Mechanics*, **3**(23), 615–617 (1986).
14. M. F. Kanninen and C. H. Popelar, *Advanced Fracture Mechanics*. Oxford Univ. Press, NY (1985).
15. D. J. Grove, Report UDR-TR-93-111, Implementation and verification of the Rajendran–Grove ceramic failure model in the 1991 research version of the Epic computer code, University of Dayton Research Institute, Dayton, OH, U.S.A. 45469–0120 October (1993).
16. G. R. Johnson and R. A. Stryk, User Instructions for the 1991 Version of the EPIC Code, Alliant Techsystems Inc., Brooklyn Park, Minnesota, Contract Report WL/MNW-TR-91-16 March (1991).
17. D. J. Grove, A. M. Rajendran, E. Bar-On and N. S. Brar, Damage Evolution in a Ceramic Rod, Shock Compression of Condensed Matter—1991. C. S. Schmidt *et al.* (eds) 971–975, Elsevier Science Publishers (1992).
18. S. Suresh, T. Nakamura, Y. Yeshurun, K.-H. Yang and J. Duffy, Tensile fracture toughness of ceramic materials: Effects of dynamic loading and elevated temperatures. *J. Am. Ceram. Soc.*, **73**(8), 2457–2466 (1990).
19. B. Budiansky and R. J. O'Connell, Elastic moduli of a cracked solid. *Int. J. Solids and Structures*, **12**, 81–97 (1976).